

One-dimensional model of a negative ion and its interaction with laser fields

R. Grobe and J. H. Eberly

Department of Physics and Astronomy, University of Rochester, Rochester, New York 14627

(Received 15 June 1993)

We describe a two-electron “atom” in one space dimension. This one-dimensional system is treated fully quantum mechanically and with full electron correlation. Its bare eigenstates and eigenenergies are determined numerically by solving Schrödinger’s equation on a spatial grid. When the electron-electron interaction (of soft-core long-range Coulombic form) is taken equal in strength and opposite in sign to the electron-proton interactions, this atom is found to have only one bound state, and is similar in other ways to a negative ion. We give a Z -correlation diagram, showing the relation of the system’s energy spectrum to those of its isoelectronic partners, which are one-dimensional analogs of He, Li^+ , etc. We also calculate a large number of fully correlated two-electron time-dependent wave functions for the system under excitation by a laser field, and exhibit a number of results, including one-photon and multiphoton photodetachment rates, ac Stark shifted threshold closings, photoelectron spectra, and above-threshold detachment spectra, single-electron and double-electron ionization probabilities, and light-scattering spectra.

PACS number(s): 32.80.Rm, 32.80.Fb, 31.20.Di, 31.15.+q

I. INTRODUCTION

In the last decade a wealth of strong-field phenomena have been observed for the first time in the multiphoton interaction of atoms and atomic electrons with strong laser pulses [1]. Even though observed in many-electron atoms, there are one-electron effects prominent among these phenomena, which include above-threshold ionization (ATI) and its related processes [2] and very-high-order harmonic generation [3]. Multielectron effects have also been observed, particularly multielectron ionization in both the multiphoton [4] and tunneling [5] regimes.

All of these experimental findings initiated theoretical calculations. The laser-atom-electron interaction is not easy to treat from a theoretical point of view. Analytic calculations are typically characterized by one or more approximations regarding the electron (classical dynamics, nonrelativistic, spinless), the atom (restricted level structure, non-Coulombic or short-range potential, featureless continua), the laser field (nonquantized, constant amplitude, zero bandwidth) and also the atom-field interaction (dipole or other inexact couplings). In order to obtain physical insight from analytical solutions further assumptions (rotating-wave approximation, perturbative or quasiclassical or Keldysh-type treatments) are unfortunately necessary.

In the domain of strong-field interactions a number of these approximations can be accepted confidently. For example, the dipole and nonquantized field approximations remain excellent. However, it is generally agreed that approximations that treat the laser intensity as constant in time, or sufficiently weak to permit perturbative calculations, must be treated very cautiously. The problem is not that such approximations always lead to errors in strong laser-atom interactions, but that their range of validity is difficult to assess. Furthermore, experimental

work is currently occurring in just the most difficult area, that of short laser pulses with high peak intensities. In reaction to these theoretical difficulties, purely numerical methods have begun to be adopted to determine atomic response, capitalizing on the availability of supercomputers and efficient algorithms that permit for the first time a direct numerical solution of the full time-dependent Schrödinger equation. Kulander [6] first presented numerical solutions for the wave functions and ionization rates of multielectron atoms using time-dependent Hartree-Fock and frozen-core methods, and we began to explore the advantages of a one-dimensional approach to one-electron strong-field processes [7], motivated by calculational efficiency and the almost exclusively one-dimensional nature of an electron’s response to a linearly polarized strong laser pulse. These and other similar efforts were based on the philosophy of testing the Schrödinger equation directly for atomic systems without dynamical or weak-field approximations in the course of its solution. In order to distinguish this from the traditional approach the numerical calculations can be called computer experiments.

Computer experiments not only provide the opportunity for confirmation of laboratory results, but also allow direct and unambiguous tests of approximate theories. Examples include a critique of the Keldysh-Faisal-Reiss (KFR) theory for photoelectron spectra [8], a check of the Bunkin-Fedorov-Kroll-Watson approximations introduced for strong-field electron-atom scattering [9], a test of the time-dependent Hartree-Fock approximation for a two-electron system [10], agreement between various predictions and observations of multiphoton effects in hydrogen [11], and parallel laboratory and computer experiments on high-order harmonic generation [12]. In addition, computer experiments have entered domains that are thus far inaccessible to laboratory experiments and in which novel phenomena are predicted to occur. Two ex-

amples are the predictions of atomic stabilization and electron localization in superstrong fields [13], and the existence of regularly-spaced “replicas” of threshold cusps in photoelectron spectra [14].

There are several reasons to expand the applications of numerical experiments. In the first place, significant improvements in approximate analytical strong-field methods are not yet in sight. Second, computer experiments for real atoms have been mostly restricted to single-electron systems so far, but laboratory studies of multielectron atoms in strong fields are being pursued vigorously. It is obvious that the behavior of multielectron atoms remains centrally interesting in strong-field physics, not only in respect to obvious questions such as the mechanism for double ionization, but even in respect to the ejection of a single electron which is affected by its correlation with other electrons. Correlation effects are strongest in the negative ions, and we have begun to study a one-dimensional analog of H^- that is a direct extension of the one-electron system mentioned already. For this analog the solution of the time-dependent Schrödinger equation can be performed on a large spatial grid, without new approximations or restrictions regarding laser pulse shape or intensity. At the same time, important progress is being made [15,16] in theoretical studies of multiphoton processes in the true three-dimensional H^- . Up to the present time, however, these are restricted to perturbative regimes of intensity, and are not yet able to address questions such as the relative roles of direct and sequential double-electron ejection pathways [17], the possibility of low-intensity stabilization regimes [18,19], or the interplay of strong-field photon dressing and electron correlation [20].

The numerical advantages of one dimension are obvious. A 1 000 000-component wave function can represent one million space points for a single electron and 1000 space points each for two electrons. This is barely sufficient to describe relatively high-energy electrons during ionization or detachment with sufficient resolution. If the system were described in two dimensions there could be only 1000 points on each axis for one electron and only 32 points on each axis for each of two electrons. For a three-dimensional system of two electrons, the 1 000 000 numerical points would permit only 10 grid points in each direction.

Of course, the physical disadvantages of a one-dimensional atom are readily apparent even in the one-electron case, where there are no angular distributions in the usual sense, circular polarization cannot be treated, there are no level degeneracies, etc. However, as is well known by now, our model has well-defined selection rules based on parity, its Coulombic potential leads to normal Rydberg spacing of high-lying bound levels, and so on, and most of the strong-field dipolar response is linear anyhow. Nevertheless, it was not clear at the outset whether a similar two-electron system would make sense as an “atom.” However, there are apparently no severe difficulties. For example, the soft core of the quasi-Coulombic potential that we use [7] permits the electrons to pass each other along the axis of motion (which is determined physically by the polarization axis of the

laser). The first strong-field results on one-dimensional two-electron systems have already appeared [10,17–20], and they are encouraging.

The main objective of this paper is to present a description of the properties of this two-electron system and also to present some details about our numerical methods. The eventual goal of our studies is to obtain a physically realistic picture of two-electron atoms responding to strong radiation fields.

The paper is organized as follows. In Sec. II we introduce the bare Hamiltonian of the two-electron system, its symmetries and its interpretations as a prototype model for negative ions. In Sec. III we mention some computational details. Section IV discusses the bare properties of the two-electron system in the absence of the laser field. We stress the universality of the model Hamiltonian and show how scaling properties can generalize our results to different two-electron systems. Section V provides a link between the static bare-atom results and time-dependent features of the fully laser-dressed two-electron wave functions. We compute the bound-free dipole moment matrix element to compare the predictions of Fermi’s golden rule with numerically observed one-photon detachment rates, and in Sec. VI we investigate detachment rates in the multiphoton regime. We confirm earlier predictions about the behavior of the rate as a function of laser intensity in the neighborhood of ponderomotive channel closings. In Sec. VII we discuss various ways of calculating photoelectron energy spectra and show various above-threshold detachment (ATD) spectra. In Sec. VIII we investigate the time dependence of single and double ionization probabilities and various bound-state populations. Section IX presents scattered light spectra in a regime of laser intensities where double ionization is significant. We close with a summary of our investigations in Sec. X.

II. THE MODEL SYSTEM FOR NEGATIVE IONS

Let us begin with a description of our two-electron system. It is characterized by a nucleus of positive charge fixed at the origin at $x=0$ and two electrons whose spatial coordinates are x_1 and x_2 . It is a one-dimensional analog of a negative ion [21] and its bare Hamiltonian is (in atomic units, a.u.)

$$H_0 = \frac{1}{2}p_1^2 + \frac{1}{2}p_2^2 + V(x_1) + V(x_2) - V(x_1 - x_2), \quad (2.1)$$

where the soft-core Coulomb potential has been chosen as

$$V(x) \equiv -\frac{1}{\sqrt{x^2 + 1}}. \quad (2.2)$$

This potential governs both the attractive electron-nucleus and the repulsive electron-electron interactions. Note that this potential permits the two electrons to move past the nucleus and past each other so the entire x axis is available to both electrons, making parity a good quantum number. In Fig. 1 we show the potential energy as a function of x_1 and x_2 . The potential is symmetric with respect to the $x_1 = -x_2$ and $x_1 = x_2$ diagonals. The spine along the line $x_1 = x_2$ indicates that it is energetically not favored to find both electrons on the same side

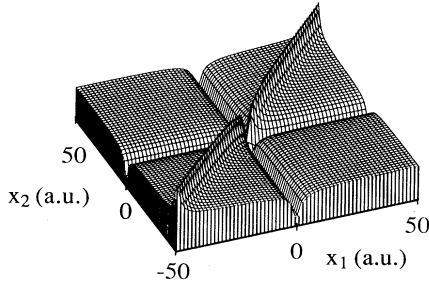


FIG. 1. The total potential $V(x_1, x_2)$ as a function of the two one-dimensional electron coordinates x_1 and x_2 .

of the nucleus. The “flat” area close to the $x_1 = -x_2$ diagonal (electrons on opposite sides of the nucleus) would be associated with the Wannier ridge [22] in the usual hyperspherical representation of the potential surface for a three-dimensional (3D) ion. The potential, and thus the bare Hamiltonian H_0 , is invariant under the two symmetry operations

$$H_0(x_1, x_2) = H_0(x_2, x_1), \quad (2.3)$$

$$H_0(x_1, x_2) = H_0(-x_1, -x_2). \quad (2.4)$$

Thus, the time-independent Schrödinger equation for the bare energies E and eigenfunctions $\Phi_E(x_1, x_2)$ can be decomposed into four noninteracting subspaces. Relation (2.3) allows for a separation into wave functions which are either symmetric or antisymmetric under exchange of the electrons’s spatial coordinate. The lowest-energy eigenstate is nondegenerate and belongs to the symmetric (spin singlet) even-parity manifold as is the case for the ground state in a three-dimensional negative ion.

The time-dependent Hamiltonian $H(t)$ that describes the interaction of the ion with a laser field is given by

$$H(t) = H_0 + (x_1 + x_2)\mathcal{E}(t)\sin(\omega t), \quad (2.5)$$

where the time-dependent term represents the dipole coupling of the two electrons to the laser’s electric field. The electric field envelope is $\mathcal{E}(t)$ and the laser frequency is denoted by ω . Given the spin independence of the laser-atom interaction, we have restricted our analysis to symmetric states corresponding to spin singlets. The second invariance (2.4) reflects a spatial parity which is the 1D counterpart to angular momentum [23]. The laser field in dipole approximation couples the corresponding odd- and even-parity subspaces. We denote by $\Psi(x_1, x_2; t)$ the general two-electron wave function that is the solution of the time-dependent Schrödinger equation.

III. TECHNICAL ASPECTS

For the purpose of solving Schrödinger’s equation numerically, the two-electron wave function is represented spatially on a two-dimensional grid where each electron’s spatial coordinate is discretized as $x_i = (-\frac{1}{2}N + i - \frac{1}{2})\Delta x$, $i = 1, 2, 3, \dots, N$. Here, $\Delta x = L/N$ denotes the grid-point spacing, L the length of the numerical box,

and N the total number of grid points inside the spatial interval $[-L/2, L/2]$. Depending on accuracy requirements L was varied between 100 and 1000 a.u., and the spatial grid spacing Δx was taken in the range 0.01–0.98 a.u. Our highest-accuracy results have been obtained for $N = 1024$ grid points, corresponding to a two-electron wave function with 1024×1024 components. Note that in such a spatial basis the corresponding Hamiltonian would have about $4(1024/4)^4$ nonzero matrix elements which because of the astronomical computer storage requirements prohibit any conventional direct diagonalization.

The time evolution of the wave function under the bare Hamiltonian H_0 is formally trivial but computationally useful in several ways. Given an initial wave function $\Phi(x_1, x_2)$, its time evolution is effected by the familiar unitary operator $U_0(t-t_0) = \exp[-iH_0(t-t_0)]$ which, for a small time increment Δt , can be decomposed into a three-step sequence by “splitting” the kinetic-energy term $T = \frac{1}{2}p_1^2 + \frac{1}{2}p_2^2$,

$$\begin{aligned} U_0(\Delta t) &= \exp[-i(T+V)\Delta t] \\ &= \exp[-iT\Delta t/2]\exp[-iV\Delta t]\exp[-iT\Delta t/2] \\ &\quad + O(\Delta t^3). \end{aligned} \quad (3.1)$$

This symmetric split decomposition is quite advantageous [24,25]. The action of the kinetic-energy operator on the wave function can be performed easily in Fourier space. It is important to note that in contrast to the usual approximations of the second derivative by three- or five-point formulas the action of the kinetic-energy operator on the spatial grid can be performed exactly here. This allows for much larger spatial grid-point spacing Δx than used with the traditional Crank-Nicholson-type methods. The application of the spatial fast Fourier transform (FFT) routine automatically leads to periodic boundaries. The middle part of the evolution operator describes the action of the potential energy alone and corresponds to a simple multiplication of the wave function in coordinate space.

The time step Δt can be chosen comparatively larger than in Crank-Nicholson-type calculations. For most simulations a time step $\Delta t \approx 0.2$ a.u. was sufficient. Programs runs consist of up to 40 000 consecutive Fourier transformations which can be performed quite efficiently on a supercomputer. We have mainly used a Cray-Y which fast-Fourier-transforms (FFT) a 1024×1024 complex matrix within about 0.56 s of CPU time by using very efficiently vectorized routines from software libraries.

The ground-state wave function $\Phi_g(x_1, x_2)$ and its energy E_g can be computed directly by replacing the time increment Δt in Eq. (3.1) by an imaginary time step $-i\Delta t$. Any arbitrary initial or “seed” wave function $\Phi(x_1, x_2)$ relaxes into the ground state after a sufficient amount of imaginary time. The wave function has to be renormalized after each integration step in order to diminish the contribution from the other eigenmodes which are contained in the initial state. The higher-lying eigenstates can be generated consecutively by the same method after the contributions of lower lying states have been

projected out of the iterated wave function at each time step. This method is accurate and reliable but it is only efficient for the determination of the lowest-lying states.

Another time-dependent method [24] that is useful in finding bare atom properties uses real-time evolution to obtain selected eigenvalues and eigenvectors, as follows. The wave function is again integrated in time using the split-operator technique and Fourier transformations of the displaced-time overlap (“autocorrelation”) function $\langle \Phi(x_1, x_2) | U_0(\tau) \Phi(x_1, x_2) \rangle$ which are performed as

$$P(E) \equiv \int_0^T d\tau \exp(iE\tau) \times \langle \Phi(x_1, x_2) | U_0(\tau) \Phi(x_1, x_2) \rangle h(\tau), \quad (3.2)$$

where $h(\tau)$ denotes the Hanning window function [24,26]

$$h(\tau) \equiv \sin^2(\pi\tau/T). \quad (3.3)$$

The peaks in the spectral function $P(E)$ correspond (for a small Δt) to the desired eigenenergies of H_0 . Due to the finite integration time T each gross eigenenergy peak consists of a multiplet of peaks closely spaced by $2\pi/T$. These additional peaks (basically sinc-type satellites) are obviously not different eigenenergies. The smooth turn on and turn off of the window function diminishes these satellite peaks. In return for that the window function broadens each spectral peak. The spectral resolution is determined by the total integration time T .

Naturally $P(E)$ can be calculated only for a finite number of discrete values in energy and one has to guess the precise locations of the maxima. In order to improve the accuracy of the peak positions we applied a line-shape fitting method [24] which makes use of the fact that the functional dependence of $P(E)$ on E is known analytically (essentially a sequence of broadened sinc functions) due to the simple form of the Hanning window. This method performs the interpolation exactly and improves the accuracy of the desired peak position by at least one significant digit.

The eigenvalues μ of the unitary operator $U_0(\Delta t)$ obviously depend on the time increment Δt . In the limit of sufficiently small Δt the imaginary part of $-(\ln\mu)/\Delta t$ becomes independent of Δt and approaches the bare energy eigenvalues E of the Hamiltonian H_0 . We have found that a time step of $\Delta t \approx 0.2$ a.u. leads to eigenvalues with a precision of three significant figures, which is sufficient for almost all practical purposes. By choosing the spatial parity of the initial seed wave function $\Phi(x_1, x_2)$ one can selectively excite either the even- or odd-parity subspace of eigenmodes. This can increase the resolution of two neighboring eigenmodes even further.

A similar spectral method can be applied to generate selected eigenvectors $\Phi_E(x_1, x_2)$ with energy E . To do this we propagate an arbitrary seed wave function $\Phi(x_1, x_2)$ in time to get $U_0(\tau)\Phi(x_1, x_2)$ and Fourier transform it as

$$c \Phi_E(x_1, x_2) \equiv \int_0^T d\tau \exp(iE\tau) U_0(\tau) \Phi(x_1, x_2) h(\tau), \quad (3.4)$$

where the constant c is to be determined by normalization. The transform can be performed after each time step Δt . The time evolution of only a single initial wave

function is already sufficient to generate several eigenvectors. With 24 megawords of computer memory we can generate simultaneously up to 40 eigenvectors on a 512×512 dimensional grid. As a “quality” check of the eigenvectors we have iterated the eigenvectors one time step Δt and determined the variance of U_0 for each one. This variance can be related to the actual energy uncertainty of that state and can be arbitrarily decreased by increasing the integration time T .

So far we have put the focus on features of the bare two-electron system. However, the wave function $\Psi(x_1, x_2; T)$ at the end of the laser pulse can be also regarded as a seed wave function, and exactly the same autocorrelation method can be applied to it equally well. This provides the energy distribution for the electrons after their interaction, including photoelectron spectra, bound-state population, etc. [27].

IV. EIGENENERGIES AND EIGENSTATES

A. The bare energy spectrum

The bare energy spectrum of our one-dimensional two-electron system is interesting in itself. We are ultimately concerned only with fully correlated two-electron energies, but we proceed through a sequence of partially correlated energies, beginning with the energies of the Hamiltonian for two completely uncorrelated hydrogen atoms. To do this we allow the coupling strength between both electrons to be a variable parameter G and define the following Hamiltonian:

$$H^G = \frac{1}{2}p_1^2 + V(x_1) + \frac{1}{2}p_2^2 + V(x_2) - GV(x_1 - x_2). \quad (4.1)$$

For the scaling parameter $G=1$, this corresponds to H_0 for our negative ion as given in Eq. (2.1).

For the special case of zero electron-electron repulsion ($G=0$) this Hamiltonian decouples into two commuting one-dimensional soft-core hydrogenic Hamiltonians whose eigenspectrum E_n has been tabulated [28]. The total energies E_{nm} of H^G for $G=0$ are simply sums of the two single-electron energies

$$E_{nm}^0 = E_n + E_m. \quad (4.2)$$

Some of the two-electron energies for the $G=0$ states with negative energy are displayed in Fig. 2(a). For graphical clarity we present only the four lowest-lying states below the first and second thresholds. The symbol (+) indicates states with even spatial parity [$\Phi(x_1, x_2) = \Phi(-x_1, -x_2)$] and (×) denotes the odd-parity states [$\Phi(x_1, x_2) = -\Phi(-x_1, -x_2)$]. Clearly, (1,1) amounts to the $G=0$ ground state with energy $E_{11}^0 = 2E_1 = -1.3396$ a.u. The states $(1, n)$ correspond to the first Rydberg series which converges to the first threshold at $E = -0.669818$ a.u. This threshold is characterized by one electron in the hydrogenic ground state and the other electron in the continuum.

The bound state (2,2) with energy $E_{22}^0 = -0.54987$ a.u. is above the first threshold and is degenerate with the continuum state $|1, \epsilon\rangle$ where ϵ is the continuum energy $\epsilon = 0.11994$ a.u. of the unbound electron. This is similar

to the situation in the corresponding three-dimensional system where the (2,2) state energy (2×-0.125 a.u.) also lies above the first threshold (which is at -0.5 a.u.) for zero electron-electron correlation.

We can calculate the spectrum for any value of G and also monitor the behavior of the eigenstates. The repulsive potential $GV(x_1-x_2)$ lifts all energies and couples states to each other. In Fig. 2(b) we compare the behavior of the energies (crosses) with the prediction of a first-order perturbation theory (open circles). The G dependence of the energies in a simplified first-order perturbation theory is given by

$$E_{nm}^G = E_{nm}^0 + G \langle \phi_n(x_1)\phi_m(x_2) | V(x_1-x_2) | \phi_n(x_1)\phi_m(x_2) \rangle, \quad (4.3)$$

where $\phi_n(x)$ denotes an uncorrelated ($G=0$) single-electron state. For small G , the slope of E^G vs G is quite well described by perturbation theory and the agreement

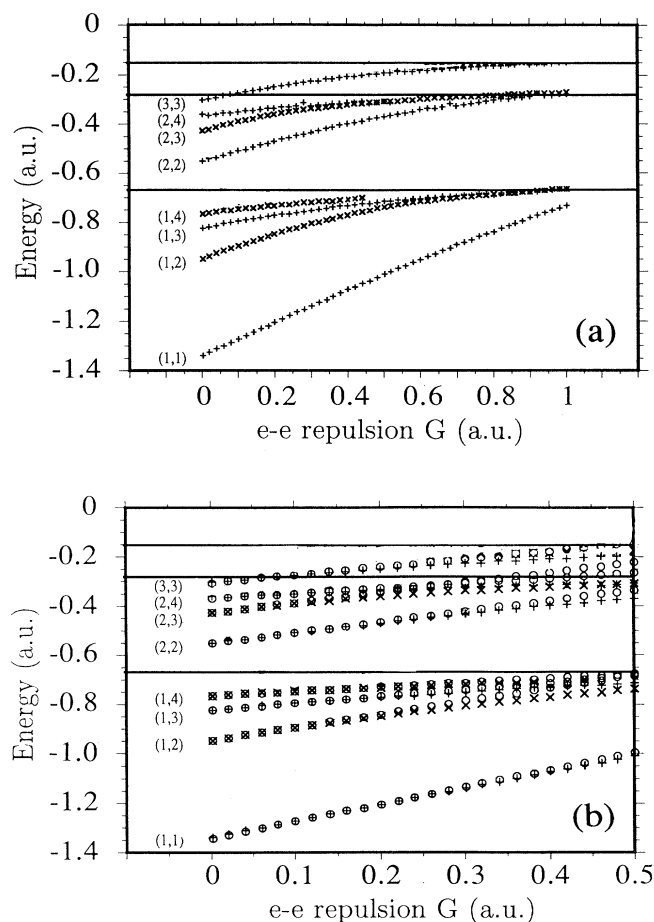


FIG. 2. (a) The total energy of the two-electron Hamiltonian (4.1) as a function of the “electron-electron repulsion strength” G . Note that the thresholds (horizontal lines) are constant and do not depend on G . The state (1,4) was not resolved beyond $G \approx 0.5$. (b) Total energy of the two-electron Hamiltonian (4.1) calculated via a simplified first-order perturbation theory [Eq. (4.3)] and shown by the open circles.

is better the farther the unperturbed states are energetically apart from each other. Note that even the (2,2) state behavior is quite nicely predicted even though our perturbation theory did not use the correct (Fano-type) re-diagonalization which would include the continuum states $|1, \epsilon\rangle$. Clearly (2,2) turns into an autodetaching state for $G \neq 0$ and approaches the second threshold as G approaches 1.

All bound levels (1, n) move closer to the threshold with increasing G . The threshold energies are unchanged by G because the thresholds reflect the bound-state structure of the core system, which is clearly the same for all G . With increasing G the positively charged nucleus is screened more and more by one of the electrons. At $G=1$ the net force on the outer electron turns into a non-Coulombic short-range force. For $G \approx 1$ the bound states accumulate at the threshold and for $G=1$ we find only one two-electron state below the threshold.

We should mention here that the spectra in Fig. 2 were calculated for each G separately. This is a very CPU time-consuming task. Therefore, we chose a larger grid and a smaller box size L than used in other calculations, and as a result the total number of bound states was small, and the thresholds might be slightly shifted (± 0.02 a.u.) from their true position.

Let us summarize our findings so far as shown in Fig. 2. As the effect of electron-electron repulsion is increased in the range $0 < G < 1$ the neutral hydrogenic system with its many bound Rydberg levels changes continuously into a negative ion with only one bound state. This is a strong confirmation, of course, that it makes sense to refer to our 1D system as a negative ion. However, with our numerical techniques we cannot completely exclude the possibility of more bound states with energies very close to the threshold [29]. The energy levels of our one-dimensional negative ion are displayed in Fig. 3. The

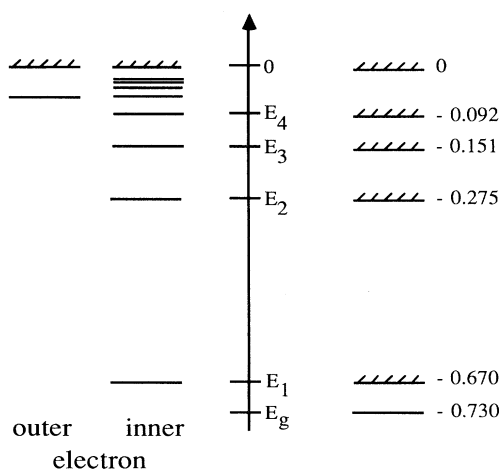


FIG. 3. The energy-level diagram based on the total two-electron energy. On the left-hand side of the vertical energy scale we show a level scheme based on a single-particle interpretation. On the right-hand side we display only the two-electron ground state and the four lowest-lying (one-electron) thresholds and the two-electron threshold, which are indicated by crosshatching. Energies are given in a.u.

two-electron threshold is at $E=0$. The system has a Rydberg series of one-electron thresholds, indicated in the rightmost column by the hatch marks, which are defined by the bound states of the core electron alone. The core ground state corresponds to the first threshold for our negative ion and it is known [28] to be at energy $E_1 = -0.669\,818$ a.u. Correspondingly, our negative ion has a detachment energy of $E_D = -0.730\,635\,8 + 0.669\,818$ a.u. = -0.0608 a.u. The second threshold, i.e., the first inelastic threshold, is at energy $E_2 = -0.274\,936$ a.u.

The level scheme in the left part of Fig. 3 presents an alternative view of the two-electron energies in single-particle terms. The left column contains the only discrete state of the weakly bound outer electron and its threshold. The right column contains the corresponding bound levels of the more deeply bound inner (core) electron.

The ratio of the energies E_1/E_D is some measure of the strength of the electron-electron correlation. It is approximately 11 for our one-dimensional model, which compares well with the known ratios for most of the alkali-metal negative ions (Li^- , Na^- , K^- , Rb^-) [21] which are also close to 10. For hydrogen the ratio is 18, which suggests that our model should compare more closely to an alkali-metal negative ion than to H^- .

B. One-dimensional isoelectronic partners of H^-

Let us return to the two-electron systems defined by H^G for G between 0 and 1. This seemingly artificial manifold can be associated with a series of different realistic two-electron systems. It can be shown easily that G formally plays the role of an effective inverse nuclear charge Z when we allow at the same time for a rescaling of the core-size parameter in the soft-core potential. To show this, let us generalize our two-electron Hamiltonian (2.1) to one with a variable core parameter a

$$H(Z, a) = \frac{1}{2}p_1^2 + \frac{1}{2}p_2^2 - \frac{Z}{\sqrt{a^2 + x_1^2}} - \frac{Z}{\sqrt{a^2 + x_2^2}} + \frac{1}{\sqrt{a^2 + (x_1 - x_2)^2}}. \quad (4.4)$$

Apart from its one-dimensional character, $H(Z, a)$ is obviously appropriate to describe a normal two-electron system, i.e., it is a 1D analog of the Hamiltonian for H^- or He or Li^+ , etc., for $Z=1, 2, 3$, etc. By factoring Z^2 from each term, and scaling the core size and both coordinates x_1 and x_2 by Z according to the formulas $a=1/Z$, $x_1=\xi_1/Z$, and $x_2=\xi_2/Z$ we easily find

$$H(Z, 1/Z) = Z^2 \left[-\frac{1}{2} \frac{\partial^2}{\partial \xi_1^2} - \frac{1}{2} \frac{\partial^2}{\partial \xi_2^2} - \frac{1}{\sqrt{1 + \xi_1^2}} - \frac{1}{\sqrt{1 + \xi_2^2}} + \frac{1/Z}{\sqrt{1 + (\xi_1 - \xi_2)^2}} \right]. \quad (4.5)$$

Clearly, the quantity in the square brackets is exactly the Hamiltonian whose eigenvalues and eigenfunctions we have been discussing in Sec. IV A if we simply relabel

$1/Z \equiv G$. To be precise, we have shown that $G^2 H(1/G, G) \equiv H^G$.

In other words, if we interpret G as the inverse nuclear charge $1/Z$ all energy eigenvalues of our model Hamiltonian H^G correspond exactly to those of the more natural Hamiltonian $H(Z, 1/Z)$ multiplied by Z^2 . That is, if we associate the energy levels for $G=1$ with H^- , then the energies for the values $G=\frac{1}{2}, \frac{1}{3}, \frac{1}{4}, \frac{1}{5}$ that are also contained in Fig. 2, can be associated with He, Li^+ , Be^{2+} , etc., with a Z -dependent cutoff parameter a . The diagram in Fig. 2 is sometimes called a “ Z -correlation diagram” and has previously been helpful in determining quantum states by perturbative methods and also to associate appropriate quantum numbers with fully correlated states [30].

C. Exact vs approximate energy calculations

In the previous section we have shown how the various G -correlated energies can be associated with an isoelectronic sequence of two-electron systems for integer values of $1/G$. This sequence of two-electron systems provides a framework within which to compare exact and approximate calculations of various atomic properties. We will restrict our analysis here to the simplest static properties, namely the ionization potentials and the ground-state energies. In order to remove Z -dependent core-size scaling from consideration, we will investigate the first five members of the isoelectronic class of Hamiltonians $H(Z, a=1)$ as defined in Eq. (4.4).

Specifically, Table I compares exact energies with those obtained from a Hartree-Fock analysis for equivalent electrons. The exact ionization potentials were obtained from a direct diagonalization of the single-electron Hamiltonian of the corresponding single-electron core system with nuclear charge Z . The exact two-electron ground-state energy was calculated via imaginary time integration as discussed in Sec. III. The details of the Hartree-Fock approximation method developed for this system by Haan are given in a separate paper devoted to a detailed discussion of one-dimensional He [31].

Clearly the ground-state energy as well as the binding energy is decreasing with increasing attractive nuclear charge Z as expected. The simple scaling shown in the previous section is not present due to the constant Coulomb cutoff parameter adopted here. The direct comparison with the predictions of the Hartree-Fock approximate scheme show that the ground-state energy of H^- agrees up to 95% with the exact value. For helium the agreement is better (99.4%) and the agreement is almost perfect for $Z=3, 4$, and 5. This tendency for better agreement as Z increases is well known.

D. The ground-state wave function

The ground state is the only bound state of the negative-ion system. We have applied imaginary time integration as well as the spectral method discussed above to calculate the ground-state wave function for our two-electron system.

TABLE I. Ground-state energies and ionization potentials as determined by Hamiltonian $H(Z, a=1)$ for the one-dimensional isoelectronic partners of our negative ion, labeled here as H^- .

Z	Ground-state energy (a.u.)		Ionization potential (a.u.)	
	Exact	Hartree-Fock	Exact	Hartree-Fock
1 (H^-)	-0.730	-0.692	0.060	0.054
2 (He)	-2.238	-2.224	0.739	0.750
3 (Li^+)	-3.896	-3.888	1.560	1.557
4 (Be^{2+})	-5.615	-5.610	2.405	2.404
5 (B^{3+})	-7.371	-7.367	3.274	3.273

In Fig. 4(a) we display the spatial probability distribution of the ground-state wave function $\Phi_g(x_1, x_2)$. It has some similarity to the ground state of the uncorrelated two-electron Hamiltonian H^0 , the simple product of the hydrogenic ground states $\phi_1(x_1)$ and $\phi_1(x_2)$. Indeed the overlap $|\langle \Phi_g | \phi_1 \phi_1 \rangle|^2$ amounts to about 78%. The logarithmic contour plot of the probability density in Fig. 4(b) gives a very strong indication of electron-electron correlation. The "butterfly" shape of the contours shows that there is an "inner" and an "outer" electron, and the sharper dents along the $x_1 = x_2$ line compared to the $x_1 = -x_2$ line show a strong $e-e$ repulsion.

E. The continuum states

In Fig. 5(a) we present $|\Phi_E(x_1, x_2)|^2$ for a typical odd-parity continuum eigenstate. Its energy is $E = -0.533$ a.u. which is roughly one third of the way between the first ($E_1 = -0.670$ a.u.) and second ($E_2 = 0.275$ a.u.) thresholds. The wave function is greatly extended close

to the $x_1 = 0$ and $x_2 = 0$ axes which indicates that one electron is still bound (close to the nucleus) while the other electron is free.

Figure 5(b) displays the corresponding effective single-electron probability density defined as

$$\rho_E(x) = \int_{-L/2}^{L/2} dx_2 |\Phi_E(x, x_2)|^2. \quad (4.6)$$

The period for $\rho_E(x)$ is very close to 6.03 a.u. (± 0.02 a.u.) in the whole spatial interval from -200 to $+200$ a.u. This means $\Phi_E(x_1, x_2)$ has a spatial period of $\lambda \approx 12.06$ a.u. corresponding to a kinetic energy of $\frac{1}{2}(2\pi/\lambda)^2 \approx 0.136$ a.u. This agrees very well with the energy difference $\Delta E \approx 0.137$ a.u. between the total energy ($E = -0.533$ a.u.) and the threshold energy ($E_1 = -0.670$ a.u.). The single-electron density $\rho_E(x)$ is normalized to 1. It is interesting to note that the partial

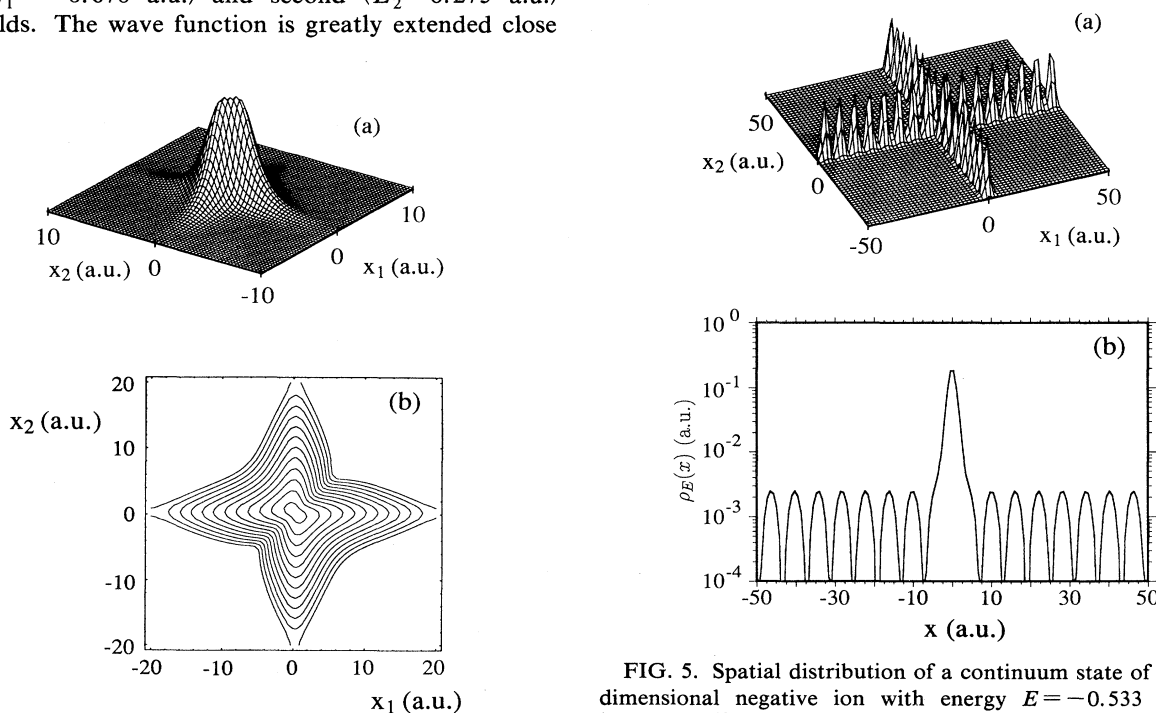


FIG. 4. The ground state $|\Phi_g(x_1, x_2)|^2$ of the one-dimensional negative ion. (a) Spatial distribution. (b) Contour plot. The 12 contours shown in the figure correspond to $|\Phi_g(x_1, x_2)|^2 = 10^{-c}$, where $c = n/2$ for $n = 5, 6, 7, \dots, 16$.

FIG. 5. Spatial distribution of a continuum state of the one-dimensional negative ion with energy $E = -0.533$ a.u. (a) $|\Phi_E(x_1, x_2)|^2$ as a function of the two spatial coordinates x_1 and x_2 . The wave function has been calculated for a box length $L = 400$ a.u., but we show it only for -50 a.u. $< x < 50$ a.u. for graphical clarity. (b) The one-electron density $\rho_E(x)$ as defined in Eq. (4.6).

area in Fig. 5(b) under the large peak at the origin (between -8 and $+8$ a.u.) is about 51% which nicely suggests that we can interpret Φ_E as a state in which one electron is bound in the core ground state and the other electron is free.

We should mention here that all energy eigenstates fulfill the “box” normalization

$$\begin{aligned} \langle \Phi_E | \Phi_{E'} \rangle &= \int_{-L/2}^{L/2} dx_1 \int_{-L/2}^{L/2} dx_2 \Phi_E^*(x_1, x_2) \Phi_{E'}(x_1, x_2) \\ &= \delta_{E, E'}. \end{aligned} \quad (4.7)$$

The average energy density of states is, therefore, not constant. The scalar product is performed on the grid via a Simpson rule which gives a satisfactory precision even for relatively large grid spacings Δx .

We have calculated all odd “continuum” eigenstates between the first and second threshold for a numerical box of length $L=400$ a.u. We found 53 odd continuum states (out of 136 odd-parity states with negative total energy) between the two lowest thresholds. The box has a grid spacing $\Delta x=0.782$ a.u. corresponding to a 512×512 grid. This size is small enough that we can resolve the eigenenergies with a reasonable amount of computing time but large enough for the quasicontinuum to be practically indistinguishable from a true continuum from a dynamical point of view. Even though a larger box size and a smaller grid spacing is computationally accessible, these choices for L and Δx are sufficient to obtain accurate bound-free dipole matrix elements.

F. Bound-free dipole moment matrix element

In the weak-field limit the negative ion’s detachment rate is proportional to the square of the dipole moment matrix element d_{gE} between the ground state Φ_g and the energy-conserving final continuum state Φ_E ,

$$\begin{aligned} d_{gE} &= \int_{-L/2}^{L/2} dx_1 \int_{-L/2}^{L/2} dx_2 \Phi_g(x_1, x_2)(x_1 + x_2) \\ &\quad \times \Phi_E^*(x_1, x_2). \end{aligned} \quad (4.8)$$

The dipole moment d_{gE} is presented as a function of E in Fig. 6 where the circles are located at the energies of the box quasicontinuum states. The dipole moment takes its

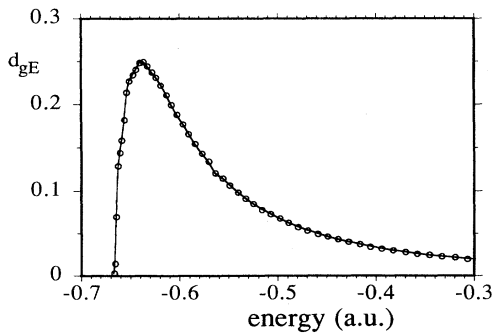


FIG. 6. The bound-free dipole-moment matrix element $\langle \Phi_g(x_1, x_2) | (x_1 + x_2) | \Phi_E(x_1, x_2) \rangle$ as a function of the continuum energy E . The circles correspond exactly to the energies of the quasicontinuum energies ($L=400$ a.u., $N=512$).

maximum value at the energy $E \approx -0.63$ a.u. which lies above the threshold by roughly half the photodetachment energy. The absolute value of these matrix elements depends on the (artificial) size of our box due to the normalization of the eigenstates in Eq. (4.7). Only when taken together with the corresponding density of states can these matrix elements be used to compute physically measurable detachment rates which are independent of the box length.

According to the different density of states in 1D and 3D negative ions, the Wigner threshold law predicts for one-photon detachment close to the threshold only a linear increase of the rate with increasing momentum for a 1D system. A detailed exploration of this regime is, however, very CPU time consuming because extremely long integration times are required to resolve the rather densely spaced states close above the threshold.

V. TIME-DEPENDENT ONE-PHOTON PROCESSES

The link between the static dipole moment matrix element and the rate of one-photon photodetachment due to a weak laser field is provided by Fermi’s golden rule (FGR). For a sufficiently weak field \mathcal{E} we would expect an exponential decay of the ground-state probability

$$P_g(t) = \exp(-R_1 t), \quad (5.1)$$

where the FGR single-photon detachment rate R_1 is given by

$$\begin{aligned} R_1 &= \mathcal{E}^2 \frac{1}{2} \pi d_{gE}^2 \rho(E) \\ &= \mathcal{E}^2 \sigma_1. \end{aligned} \quad (5.2)$$

Here, $\rho(E)$ denotes the average density of states, the inverse energy spacing of two neighboring continuum states of odd parity, and σ_1 is the one-photon detachment cross section.

To evaluate the “atomic” constant σ_1 we can use the data in Fig. 6. To be more specific, a photon energy of $\omega=0.2$ a.u. would excite the state with continuum energy $E = -0.730 + 0.20 = -0.530$ a.u., which corresponds closely to the energy of the continuum eigenstate discussed in Sec. IV E. The dipole-moment matrix element for $E = -0.53$ a.u. has the value $d_{gE} \approx 0.297$ a.u. The spacing between two neighboring eigenstates at that energy is 0.0083 a.u. With these data we can predict the value $\sigma_1 \approx 16.65$ a.u. The corresponding cross section for the real three-dimensional hydrogen negative ion lies between 12.5 and 0.5 a.u. for photon energies between 0.086 and 0.375 a.u. This is remarkably similar to the range of cross sections for the one-dimensional analog despite the different state densities and dimensionalities.

Of course, the FGR rate is not reliable in strong fields. It may fail to give an accurate estimate for many related reasons: thresholds shifts, high-order processes, distorted bare wave functions, etc., are all manifestations of strong-field excitation. This is the case of main interest to us, and the only suitable approach is through the exact time-dependent wave function for the two electrons. This wave function, denoted $\Psi(x_1, x_2; t)$, is the solution to

Schrödinger's equation with the Hamiltonian that was already given in Eq. (2.5),

$$i \frac{\partial \Psi(x_1, x_2; t)}{\partial t} = [H_0 + (x_1 + x_2) \mathcal{E}(t) \sin(\omega t)] \times \Psi(x_1, x_2; t). \quad (5.3)$$

In most of our calculations of photoinduced processes $\mathcal{E}(t)$ is modeled by a trapezoidal pulse which is turned on and off linearly over two optical cycles and in between has a plateau of constant amplitude [32]. This pulse shape minimizes ionization due to the turn-on alone. For the intensity range of interest here the laser magnetic field can be neglected and the dipole approximation is well justified. The time evolution is performed with the more advantageous velocity gauge, from which the wave function can be transformed back into the length gauge to calculate the required projections.

In order to investigate the intensity dependence of the detachment we have numerically calculated $\Psi(x_1, x_2; t)$ for laser pulses of several intensities. In order to avoid strong temporal oscillations due to counter-rotating terms we have calculated the ground-state probability

$$P_g(t) = |\langle \Phi_g(x_1, x_2) | \Psi(x_1, x_2; t) \rangle|^2 \quad (5.4)$$

with the time-dependent wave function in the velocity gauge [33]. In the constant-intensity region between the second and fourth cycle we have monitored the time dependence of the ground-state probability and determined the detachment rate as well as the deviation from a purely exponential decay by linear regression. In case of stronger fields it is also helpful to monitor the survival probability of the ground state after the pulse has been switched off (also over two optical cycles).

A more efficient computation can be achieved by using a smooth mask function which allows a reduction of the box size L and a smaller number of spatial grid points [34]. In our calculations the mask function was multiplied with the wave function at every tenth integration time step to eliminate that portion of the wave function which evolved beyond a certain distance D away from the nucleus. For large enough D , this portion can be clearly associated with the detachment; it does not influence the population in the ground state. More specifically, we have again chosen a Hanning-type mask function $M(x_1, x_2) \equiv m(x_1)m(x_2)$ where

$$m(x) \equiv 1 + \{\cos[\pi(|x| - D)/(2D)] - 1\} \Theta(|x| - D) \quad (5.5)$$

and the "cutoff" distance D was chosen to correspond to a quarter of the total box size L . We should note here that this smoothed cutoff procedure cannot be applied in simulations for which the double-ionization rate or energy spectra are of interest. The mask function reduces the norm of the wave function, which could be misinterpreted as double ionization.

In Fig. 7 we show detachment rates (open circles) as well as the final ground-state population after the pulse (diamonds) as a function of the field strength \mathcal{E} for $\omega = 0.2$ a.u. For low intensities the rates are on the

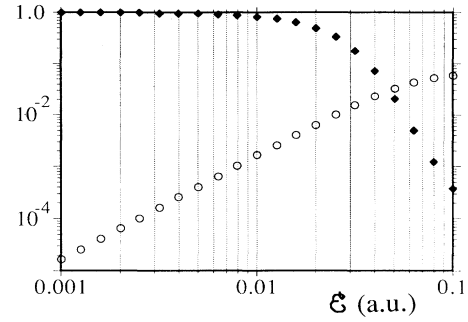


FIG. 7. The ground-state decay rate (open circles) and the final ground-state probability (diamonds) after the pulse as a function of the field strength \mathcal{E} for nominally one-photon ionization ($\omega = 0.2$ a.u., two optical cycles turn on and off, six cycles total pulse duration).

straight line that corresponds to the prediction by Fermi's golden rule (5.2). Up to $\mathcal{E} \approx 0.04$ a.u., the agreement with (5.2) is practically perfect given the value $\sigma_1 = 16.65$ a.u. already calculated. Only a very small extra intensity dependence is present. To be more specific, we have divided all rates for field strengths smaller than 0.01 a.u. by the corresponding intensity \mathcal{E}^2 and found the cross section to decrease monotonically from 16.82 (at $\mathcal{E} = 0.001$ a.u.) to 16.39 (at $\mathcal{E} = 0.01$ a.u.). This means that the discrepancy between the prediction by FGR and the actual rate is less than 2% for the whole range of two orders of magnitude in intensity. This may be the first demonstration of the range of applicability of the FGR in describing time-dependent decay in a multielectron system for which the $e-e$ interaction is fully taken into account.

Beginning at roughly $\mathcal{E} = 0.04$ a.u. the discrepancy between the rate predicted by FGR and the measured rate increases appreciably. The perturbative estimate via the FGR clearly neglects all higher-order processes, and these become important for high field strengths, and the ground-state decay becomes oscillatory with twice the laser frequency. The ground state is almost completely depleted after fewer than six optical cycles. Similar simulations with single-electron model systems found approximately a similar intensity range at which the FGR breaks down.

VI. MULTIPHOTON DETACHMENT RATES

In this section we will study the photodetachment rates [35] for a smaller laser frequency ($\omega = 0.04$ a.u.). In this case the outer electron can detach in the weak-field limit only with the absorption of at least two photons. In the next section we will discuss the corresponding photoelectron spectra for this same case. Single-active-electron theory [36–39] predicts characteristic minima in the photodetachment cross section to occur at specific laser intensities, where decay channels become closed due to field-induced level shifts. This is shown in Fig. 8(a). The question we try to address here is whether these minima can occur at all when the core electron is allowed to participate in the dynamics.

In Fig. 8(b) we present our results for the rate as well as for the final ground-state probability as a function of the laser field strength \mathcal{E} . In the weak-field limit ($\mathcal{E} < 0.008$ a.u.) the linear behavior in the double logarithmic plot indicates a clear power-law dependence of the rate on the field strength. The measured slope is 3.73 which is close to the expected dependence $R_2 \sim \mathcal{E}^4$ for a perturbative nonresonant two-photon decay [40]. At slightly higher-field strengths, close to $\mathcal{E} = 0.01$ a.u., the rate drops appreciably and deviates drastically from a simple power law. This obviously corresponds to the maximum found in the final ground-state population at the same field strength.

At much higher field strengths the concept of a detachment rate becomes meaningless and we give a rate curve only up to $\mathcal{E} = 0.013$ a.u. Beyond this value we plot only P_g at the end of the pulse. It has been suggested previously [36–39] and also partly confirmed experimentally [41] that the extrema shown for high fields in Fig. 8(b) can be associated with photodetachment channel closings. These occur, if we assume that we can neglect any shifts due to polarization effects or effects due to a (possibly) active inner electron, because the threshold energy

increases by the free-electron jitter energy (the so-called the ponderomotive energy). Channel closings should be thus expected at critical field strengths \mathcal{E}_n at which the n -photon decay channel becomes closed,

$$n\omega = |E_D| + \frac{\mathcal{E}_n^2}{4\omega^2}, \quad (6.1)$$

where $|E_D|$ denotes the positive photodetachment potential. In order to check this simplified estimate we have marked the field strengths \mathcal{E}_n in Fig. 8(b) with arrows. The agreement between the maxima in the final ground-state population and the predicted field strengths \mathcal{E}_n is qualitative but systematic. The agreement is not expected to be better because on average the ground state experiences a smaller field than \mathcal{E}_n due to the turn on and turn off of the pulse, whereas Eq. (6.1) assumes a constant intensity throughout the pulse. In any case, there is a clear one-to-one correspondence between the arrows and the maxima through the first six channel closings. It suggests that the inner electron is quite inactive in this parameter regime. To investigate the influence of the core electron on threshold shifts more detailed studies are required.

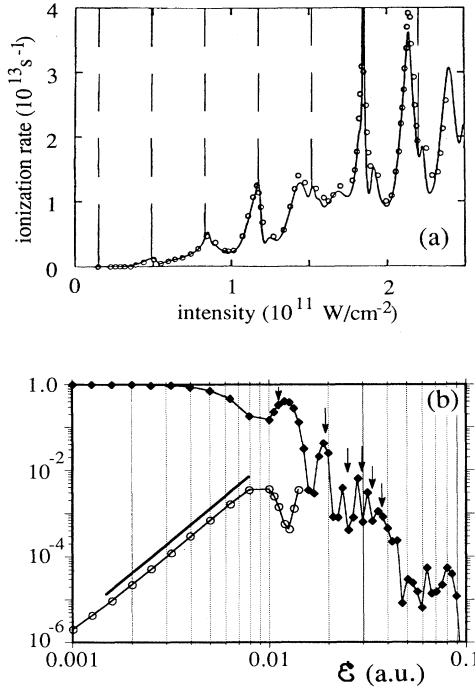


FIG. 8. (a) This is the original Fig. 8(b) from Ref. 38 [used with permission of the authors]. Ionization rate vs intensity for $\hbar\omega = 0.17$ eV. The circles are approximate reproductions of the results of Ref. [37], which were computed from a finite-range potential in one dimension. The vertical dashed lines mark the predicted intensities for channel closings. (b) The ground-state decay rate (open circles) and the final ground-state probability (diamonds) after the pulse as a function of the field strength \mathcal{E} . The arrows correspond to the field strengths \mathcal{E}_n defined in Eq. (6.1). The straight line has a slope of about 3.7 ($\omega = 0.04$ a.u., two optical cycles turn on and off, six cycles total pulse duration).

VII. PHOTOELECTRON SPECTRA AND ABOVE-THRESHOLD DETACHMENT (ATD)

The two-electron wave function $\Psi(x_1, x_2; T)$ contains all of the information available after the system has interacted with the laser pulse, including the photoelectron energy spectrum. The total (two-electron) energy spectrum $P^{(2)}(E)$ is unambiguously defined as the squared overlap of the wave function $\Psi(x_1, x_2; T)$ with the energy eigenstate $\Phi_E(x_1, x_2)$,

$$P^{(2)}(E) = |\langle \Phi_E | \Psi(T) \rangle|^2. \quad (7.1)$$

It can be determined accurately by the methods already discussed in Sec. III. When multiplied by the average density of states, $P^{(2)}(E)$ yields true energy distributions of the two-electron system, but is not obvious how to design simple laboratory detection of two photoelectrons with total energy E . It is more interesting to investigate how the total energy is distributed between the electrons.

A “single-electron” energy distribution is experimentally more easily accessible, but is more difficult to define from a theoretical point of view. In order to calculate the (single) electron energies following the pulse, the ground-state contribution was removed from the final wave function and the remainder $\hat{\Psi}(x_1, x_2; T)$ was Fourier decomposed into its momentum amplitudes $\chi(k_1, k_2; T)$,

$$\chi(k_1, k_2; T) \equiv \iint dx_1 dx_2 \exp[i(k_1 x_1 + k_2 x_2)] \times \hat{\Psi}(x_1, x_2; T), \quad (7.2)$$

where k_1 and k_2 denote the momenta. An effective single-electron energy density $P^{(1)}(E)$ can be defined as the integral of $|\chi(k_1, k_2; T)|^2$ over one of the momenta, say k_2 , and a subsequent transformation to energy via $E \equiv \frac{1}{2}k_1^2$

$$P^{(1)}(E) \equiv (2E)^{-1/2} \int dk_2 |\chi(k_1, k_2; T)|^2. \quad (7.3)$$

This definition mimics the distribution of kinetic energies of electrons which arrive at detectors far away from each other and from the nucleus. But a word of caution should be applied. In case of single-electron detachment close to zero energy the distribution $P^{(1)}(E)$ also contains the Fourier components of the bound inner electron, which prohibits a clear interpretation at small energies. However, the single-electron energy distribution between the first and second threshold can also be calculated from the total-energy distribution $P^{(2)}(E)$ even in the near threshold region.

We have previously presented [17,20] two-electron and one-electron photospectra. An investigation of one-electron peak intensities as a function of the laser pulse duration revealed the presence of previously unsuspected differential growth rates among the photoelectron peaks. The spectra shown here in Fig. 9 correspond to excitation with a high-frequency photon and a strong short pulse ($\omega=1$ a.u., pulse duration 50 optical cycles and field strength $\mathcal{E}=0.5$ a.u.). The total (two-electron) energy spectrum of Fig. 9(a) shows equidistant peaks spaced by the photon energy ω , which indicates that the negative ion has absorbed an integer number of photons. It is not clear from $P^{(2)}(E)$ alone how the energy is distributed between the two electrons. The single-photon spectrum of Fig. 9(b) shows a repeating ATD sequence labeled $s=0$, $s=1$, etc. The details of the four-peak structure within each ATD peak have been presented in higher resolution

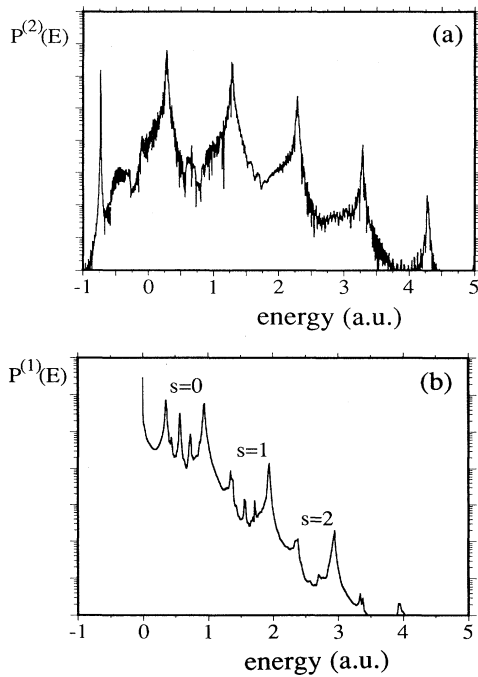


FIG. 9. (a) The distribution of the total energy $P^{(2)}(E)$ after the pulse. (b) The one-electron photospectrum $P^{(1)}(E)$ taken from the same wave function as in (a) ($\mathcal{E}=0.5$ a.u., $\omega=1.0$ a.u., two optical cycles turn on and off, total pulse duration 50 optical cycles, $L=800$ a.u., $N=1024$).

elsewhere, and have been correlated with direct and sequential one-electron and two-electron removal processes [17].

Now we turn our attention to the way one-photon ATD spectra are affected by the channel closings discussed in Sec. VI. For our example we have again chosen pulses which are linearly turned on and off over two optical cycles and have a constant-intensity plateau of 6 cycles in between, with the same low frequency $\omega=0.04$ a.u. [42].

We have already mentioned that the single-electron energy distribution between the first and second threshold can be calculated from the total-energy distribution $P^{(2)}(E)$ even in the near threshold region. In Fig. 10(a) we present $P^{(2)}(E)$ and we have shifted the energy E such that the new zero coincides with the first threshold. The energies can be interpreted as kinetic energies of the detached electron. The first three ATD spectra for $\mathcal{E}=0.005$, 0.008, and 0.010 a.u. show a sequence of photoelectron peaks which are spaced by the photon energy $\omega=0.04$ a.u. as expected, due to the absorption of additional photons. In the perturbative weak-field limit the position of the first peak should occur at continuum energy $E_g + 2\omega$ (about 0.02 a.u. above the threshold) which agrees with the position found for the lowest laser intensity. With increasing field strength our calculations indicate a redshift of the peaks toward the threshold, as expected.

However, Fig. 10(a) also shows that as we approach the channel closing intensity at $\mathcal{E}\approx 0.011$ a.u. the spectra become very sensitive to the field strength as was already noted in single-active-electron calculations [37]. The first ATD peak is drastically diminished and the second and third peak are dominant. This sensitivity is also obvious from the qualitative change of the spectra from $\mathcal{E}=0.011$ to $\mathcal{E}=0.012$ a.u. We can compare these ATD spectra directly with corresponding plots of the time-dependent decay of the ground state, which is the same thing as the detachment probability since there is only one bound state.

In Fig. 10(b) we present the detachment probabilities for the same six laser field strengths. Recall that Fig. 8(b) shows that in this range the amount of detachment first increases (for \mathcal{E} 's up to $\mathcal{E}=0.009$ a.u.), then decreases (for \mathcal{E} 's up to $\mathcal{E}=0.013$ a.u.), and then increases again for higher-field strengths, until the next channel-closing intensity (close to $\mathcal{E}=0.020$ a.u.) is reached. This behavior is apparent at $t=10$ cycles in the curves in Fig. 10(b) too, of course. [The strong oscillations apparent in the six graphs in Fig. 10(b) occur with twice the laser frequency and can be associated with counter-rotating effects. Attention can be focused on the locus of minima, which goes smoothly into the final value at the end of the pulse.] The sensitivity of the detachment process to field strength near the channel closing is again evident. For both $\mathcal{E}=0.011$ and 0.012 a.u., the decay curve (growth of photodetachment probability) suggests that at least two different times scales are determining the decay for laser fields close to the channel closing. Note that the ground state decays very weakly between the $2-\frac{1}{2}$ and $4-\frac{1}{2}$ cycle points but more rapidly in the remaining part of the con-

stant intensity plateau, particularly for $\mathcal{E}=0.012$ a.u.

We complete this section with a comparison with the time-dependent decay curves obtained previously [18,19] for the higher-frequency $\omega=0.08$ a.u. In this case, for laser intensity close to $\mathcal{E}=0.02$ a.u., a window was identified in which the inner electron is passive and allows dynamical stabilization of the outer electron. The corresponding time-dependent probabilities reported for

the stabilization window resemble those shown here in Fig. 10(b) for the intensity between $\mathcal{E}=0.010$ and 0.012 a.u. It is important that the channel-closing scenario and the increased ground-state population after the pulse (accompanying a greater pulse intensity as the channel closes) should not be confused with dynamic stabilization of [18,19]. The channel-closing scenario is found for a regime for which the ATD peaks are red shifted and it has

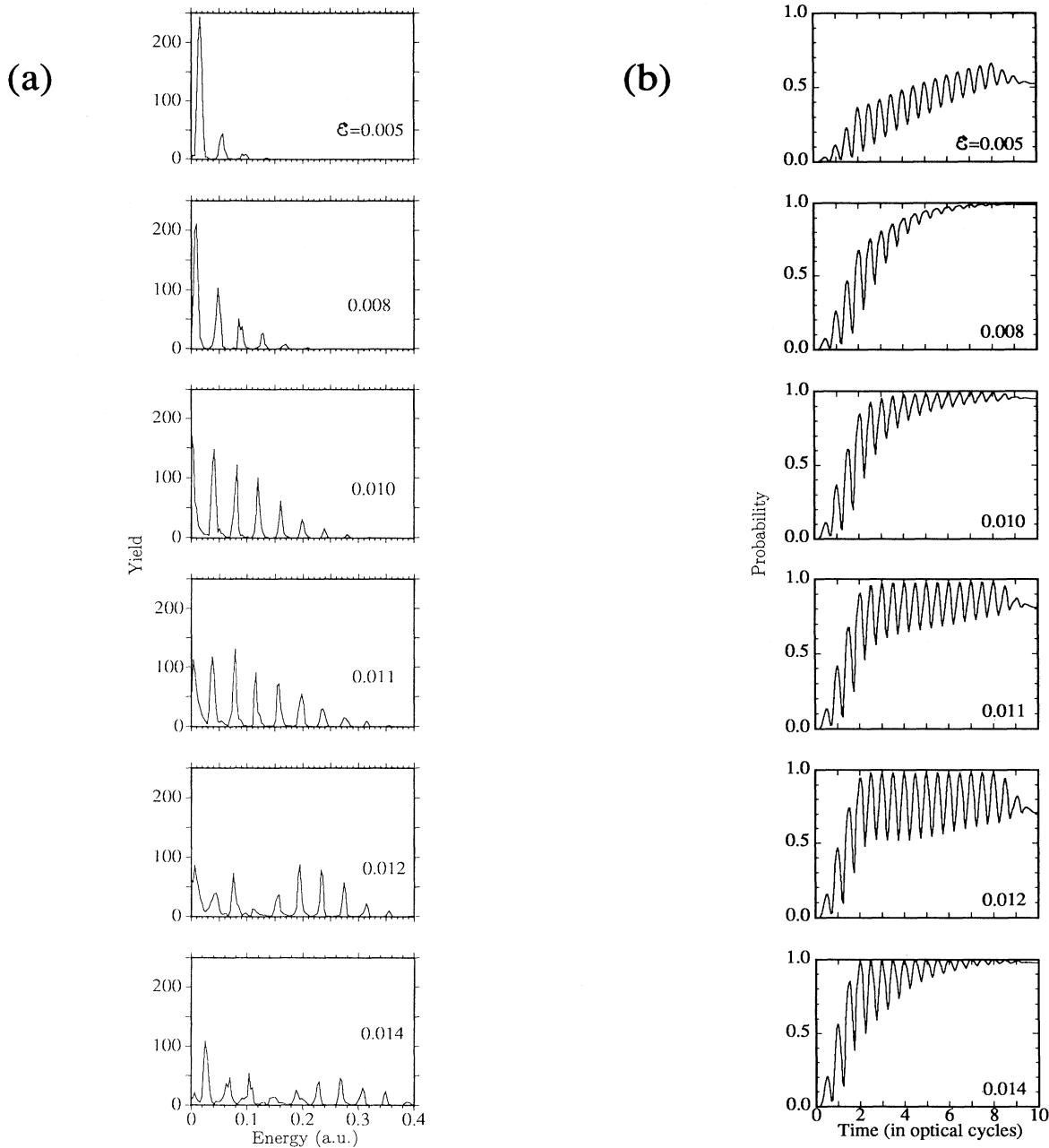


FIG. 10. (a) Photoelectron spectra obtained from the same pulses as in (b). (b) Detachment probabilities as a function of time for six laser field strengths \mathcal{E} (in a.u.). ($\omega=0.04$ a.u., two optical cycles turn on and off, total pulse duration ten optical cycles, $L=800$ a.u., $N=1024$.)

been predicted previously that stabilization should be accompanied by a blue shift [43].

In the higher-frequency ($\omega=0.08$ a.u.) case the inner electron destroys stabilization for the outer electron with increasing field strengths. For the lower-frequency case ($\omega=0.04$ a.u.) we find that even for the highest-field strength ($\mathcal{E}=0.014$ a.u.) the probability for double ionization after the pulse is always far below 1%. Clearly, the increase of the detachment probability from $\mathcal{E}=0.012$ to 0.014 a.u. is not due to the dynamical influence of the inner electron.

VIII. SINGLE AND DOUBLE IONIZATION, TIME DEPENDENCE OF VARIOUS STATES

The one-electron ionization probability, which we denote by $P^{(1)}(t)$, can be unambiguously calculated from the projection of the time-dependent wave function $\Psi(x_1, x_2; t)$ on the (two-electron) ground state $\Phi_g(x_1, x_2)$

$$P^{(1)}(t) \equiv 1 - |\langle \Phi_g(x_1, x_2) | \Psi(x_1, x_2; t) \rangle|^2. \quad (8.1)$$

In the context of our negative ion, $P^{(1)}(t)$ could also be called the detachment probability.

Let us now define another helpful projection on a single-electron state. $P_n(t)$ is defined as the probability to find (at least) one electron in the hydrogenic bound state $\phi_n(x)$. It can be calculated from the corresponding projection of the two-electron wave function $\Psi(x_1, x_2; t)$ on $\phi_n(x)$,

$$\begin{aligned} P_n(t) &= 2 \int dx_2 \left| \int dx_1 \phi_n(x_1) \Psi(x_1, x_2; t) \right|^2 \\ &\quad - \left| \int dx_1 \int dx_2 \phi_n(x_1) \phi_n(x_2) \Psi(x_1, x_2; t) \right|^2 \\ &= \langle \Psi(x_1, x_2, t) | \hat{P}_n | \Psi(x_1, x_2; t) \rangle, \end{aligned} \quad (8.2)$$

where the projection operator \hat{P}_n of the second line is defined as

$$\begin{aligned} \hat{P}_n &= (|n\rangle\langle n|)_1 \otimes \Pi_2 \\ &\quad + \Pi_1 \otimes (|n\rangle\langle n|)_2 - (|n\rangle\langle n|)_1 \otimes (|n\rangle\langle n|)_2 \end{aligned} \quad (8.3)$$

$$\begin{aligned} P^{(2)}(t) &\equiv 1 - \left\{ 2 \sum_n \int dx_2 \left| \int dx_1 \phi_n(x_1) \Psi(x_1, x_2; t) \right|^2 - \sum_{n,m} \left| \int \int dx_1 dx_2 \phi_n(x_1) \phi_m(x_2) \Psi(x_1, x_2; t) \right|^2 \right\} \\ &= 1 - \left\{ \sum_n P_n(t) - \sum_{\substack{n,m \\ n \neq m}} \left| \int \int dx_1 dx_2 \phi_n(x_1) \phi_m(x_2) \Psi(x_1, x_2; t) \right|^2 \right\}. \end{aligned} \quad (8.4)$$

The terms in the first sum describe the probabilities $P_n(t)$ that the electron with coordinate x_1 is in bound state ϕ_n independent of the other electron. The factor 2 reflects the symmetry of the wave function under exchange of the electrons' coordinates. In order to avoid double counting we have to subtract in the double sum the probability that both electrons are bound.

and Π_i denotes the unit operator acting on the i th coordinate of the wave function.

We should add here four remarks about peculiarities encountered interpreting the probabilities $P_n(t)$.

(1) The probability $P_n(t)$ is not necessarily constant even in the absence of a laser field. To give an example let us assume that the system is initially prepared in the lowest autodetaching state: $\Psi(x_1, x_2; 0) = \phi_2(x_1) \phi_2(x_2)$. Clearly, the probability of finding at least one electron in the core ground state $\phi_1(x)$ is initially zero. However, after one electron has autodetached and the other electron has "dropped" into the core ground state $\phi_1(x)$, $P_1(t)$ takes a nonzero value [31].

(2) The value of P_1 in the H^- ground state is only 97% for our model, and P_3 is already 17%. This shows that the ground state cannot be interpreted very strictly as a weakly bound outer electron and a core electron in the exact hydrogenic state $\phi_1(x)$.

(3) The expectation value of the sum of all projectors $\sum_n \langle \hat{P}_n \rangle$ can exceed 1 because the probabilities $P_n(t)$ are not mutually exclusive, and the product of two different projectors $\hat{P}_n \hat{P}_m$ is always nonzero.

(4) In the special case of two noninteracting electrons [take $G=0$ in Eq. (4.1)] the expectation value $P_n(t)$ does not reduce to the simple probability $|\langle \phi_n | \psi(t) \rangle|^2$, where $\psi(t)$ denotes the wave function of the corresponding single-electron problem. It should be more appropriately interpreted as the probability that at least one electron is in state $\phi_n(x)$ under the assumption that we have *two hydrogen atoms* at our disposal: $P_n(t) = 2|\langle \phi_n | \psi(t) \rangle|^2 - |\langle \phi_n | \psi(t) \rangle|^4$.

Another quantity of physical interest is the double-electron ionization probability $P^{(2)}(t)$. The definition of double-electron ionization is not straightforward from a conceptual point of view. Even within the classical context it is not clear how one can uniquely define a double-ionization probability for a three-body system. In quantum-mechanical language, an electron state of positive total energy is not necessarily equivalent to two unbound electrons. We will *define* $P^{(2)}(t)$ as the probability that neither of the two electrons is in a bound state of the corresponding hydrogenic core (see the Appendix). The latter is obviously the complement of the probability that at least one electron is in a hydrogenic bound state $\phi_n(x)$,

We have calculated examples of the probabilities defined in the previous section for our negative-ion model. We have chosen the laser frequency $\omega=1.0$ a.u., which is large enough to doubly ionize the atom under the absorption of only one photon. The laser field strength was 0.5 a.u. and the corresponding photoelectron spectra have already been presented in Fig. 9.

We show in Fig. 11 the single-ionization probability $P^{(1)}(t)$ and the double-ionization probability $P^{(2)}(t)$ as a function of time. These probabilities actually oscillate strongly with twice the laser frequency, corresponding to the jitter motion of the electrons. The size as well as the phase of these oscillations during the pulse depend on the gauge of the wave function [33]. To avoid any confusion and to improve graphical clarity we have shown only the minima in the figure. The locus of these minima behaves smoothly even during the turn off (from the 48th optical cycle to the 50th) and goes continuously over into the probabilities after the pulse. It is apparent from Fig. 11 and also in agreement with previous findings [17] that the “first” electron escapes on a much shorter time scale than the “second” electron. After the first 6 optical cycles of the laser pulse the two-electron ground state has already decayed by almost half whereas the double-ionization probability needs roughly 30 cycles to decay by half. Note that in contrast to the single ionization, the temporal behavior of the double ionization $P^{(2)}(t)$ cannot be described by a simple exponential. The question whether the rapid ground-state decay is due to the inner or outer electron has been investigated in previous work [17]. These two ionization probabilities themselves do not allow any elaborate interpretation of the various mechanisms involved in the decay.

More information can be obtained from Fig. 12 where we display the “core state” probabilities $P_n(t)$ as defined in Eq. (8.2). Again we present only the probability minima of the curves. $P_1(t)$, the probability to find at least one electron in the core ground level, is 97% at $t=0$ as mentioned in Sec. VIII and decays on a time scale intermediate between the ones for $P^{(1)}(t)$ and $P^{(2)}(t)$.

$P_2(t)$ vanishes before the laser pulse, but during the two cycle turn on of the laser the $n=2$ core level becomes appreciably populated and reaches almost 50%. This probability then decays to 20% after 12 cycles. During the remaining 38 cycles of the pulse $P_2(t)$ remains almost constant and the population seems to be trapped in that core state. This is interesting because the odd-parity core-electron state $\phi_2(x)$ is not directly dipole

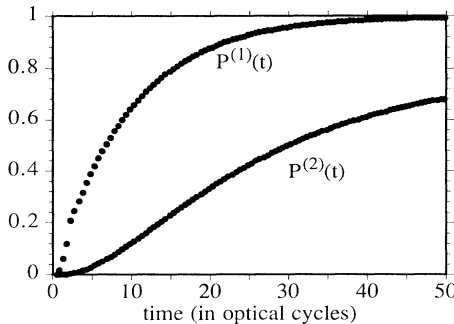


FIG. 11. The ionization probability for single-ionization $P^{(1)}(t)$ and for double-ionization $P^{(2)}(t)$ as a function of time. Wide oscillations occur every half-cycle, but we have shown only the minima for graphical clarity. The laser pulse is the same as used in Figs. 9 ($\mathcal{E}=0.5$ a.u., $\omega=1.0$ a.u., two optical cycles turn on and turn off).

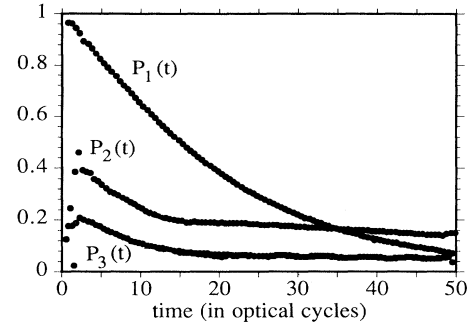


FIG. 12. The time dependence of the “core-state” probabilities $P_n(t)$ as defined in Eq. (8.2) for the same laser pulse as in Fig. 9. We show only the maxima of the curves. The initial probability for $P_2(t=0)$ is negligible, whereas $P_3(t=0)$ is 17% in the two-electron ground state ($\mathcal{E}=0.5$ a.u., $\omega=1.0$ a.u., two optical cycles turn on and turn off, total pulse duration 50 optical cycles).

coupled to the core ground level. It is not clear if that trapped portion should be associated with strong-field stabilization. The population in the $n=3$ core level shows a similar behavior. It gains most of its population during the turn on, loses roughly half of it during the next 10 cycles and then ceases to decay during the remainder of the pulse.

It is not unexpected that the core shake up, producing transitions to the first two excited core states $n=2$ and 3, occurs during the pulse turn on. Furthermore, $P_1(t)$ and $P_2(t)$ decay on two different time scales. The most rapid time scale corresponds to the time on which the two-electron ground state decays. This suggests that due to electron-electron collisions the core-electron can be “knocked out” by the outer electron. When the outer electron has become detached the core electron state decays on a very slow time scale. These findings suggest that our photoelectron spectra, which obviously depend strongly on the core state populations, are much more sensitive to turn-on effects than the corresponding spectra for single-electron systems.

IX. THE SPECTRUM OF SCATTERED LIGHT

In this section we discuss briefly the spectrum of the scattered light generated by the interaction of our negative-ion model with a strong laser field. A more thorough analysis will be presented elsewhere [44]. The photon spectrum depends on the time-dependent dipole moment $\langle x_1 + x_2 \rangle$, or more directly on the expectation value of the acceleration $\langle \ddot{x}_1 + \ddot{x}_2 \rangle$:

$$\langle \ddot{x}_1 + \ddot{x}_2 \rangle = \left\langle -2\mathcal{E}(t)\sin(\omega t) - \frac{\partial}{\partial x_1} V(x_1, x_2) - \frac{\partial}{\partial x_2} V(x_1, x_2) \right\rangle. \quad (9.1)$$

Due to the symmetry of the two-electron wave function it is sufficient to compute the acceleration of only one electron. In practice we have calculated the spectrum from

the Fourier transform of the time-dependent expectation value of the single-electron force $\langle -(\partial/\partial x_1)V(x_1) \rangle$. Even though both electrons are strongly correlated the contribution of the repulsive two-electron force to the acceleration of the expectation value is zero.

There is one further advantage in using the expectation value of the force. As opposed to the dipole operator, which takes its maximum value at the (unphysical) boundaries of the numerical box, the force is centered around the origin and falls off rapidly towards the boundaries. This leads to photon spectra which are less influenced by an interaction of the wave function with the boundary. We have found that interaction with the boundaries can lead to artificial even and odd harmonics of the laser field of very high order. Comparative simulations, for which the mask function discussed in Sec. V was used, allow identification of “unphysical” contributions in the spectra.

We will present light spectra generated by a low-frequency ($\omega=0.08$ a.u.) laser pulse and a range of field strengths between $\mathcal{E}=0.01$ to 0.08 a.u. We have found in previous work with the same frequency photons that this range of field strengths is particularly interesting in the sense that the negative ion undergoes a transition from dominantly single to dominantly double ionization around $\mathcal{E}=0.04$ a.u. The corresponding time-dependent probabilities for this case have been discussed elsewhere [19,20].

Figure 13 shows four photon spectra, corresponding to laser fields of increasing strength. Figure 13(a) shows the harmonic spectrum obtained for the lowest field strength ($\mathcal{E}=0.01$ a.u.) and a pulse of 18 optical cycles. This field is strong enough to detach the outer electron rapidly. The ground state probability drops by half during the first two cycles of the turn on and goes to zero after only 8 cycles. The light spectrum contains clear evidence of only the third and fifth harmonics in addition to the main peak at the laser frequency.

The intermediate intensity range around $\mathcal{E}=0.02$ a.u. is more interesting. We have shown [18,19] that the field is strong enough to stabilize the outer electron but not strong enough to ionize the core electron. The double-ionization probability is still negligible after such a pulse. Figure 13(b) shows the harmonic spectrum in this single-electron-stabilization regime. The highest harmonic clearly identifiable in the light spectrum is the fifteenth. We should note that the harmonics fall off monotonically with increasing order and that there is no plateau evident in the figure.

The third intensity regime around $\mathcal{E}=0.08$ a.u. is characterized by very rapid detachment and an appreciable amount of double ionization. We have found that after the laser pulse the negative ion has decayed to the neutral hydrogen core in its ground level (30%) and to a nucleus with two free electrons (70%). The light spectrum in Fig. 13(c) shows the presence of odd harmonics with maximum order around 27. This time one can recognize an extended harmonic plateau up to the 19th or 21st harmonic and a rapid cutoff after that. The amplitudes in the plateau region show some weak oscillatory structure. It was not clear at the two lower intensities

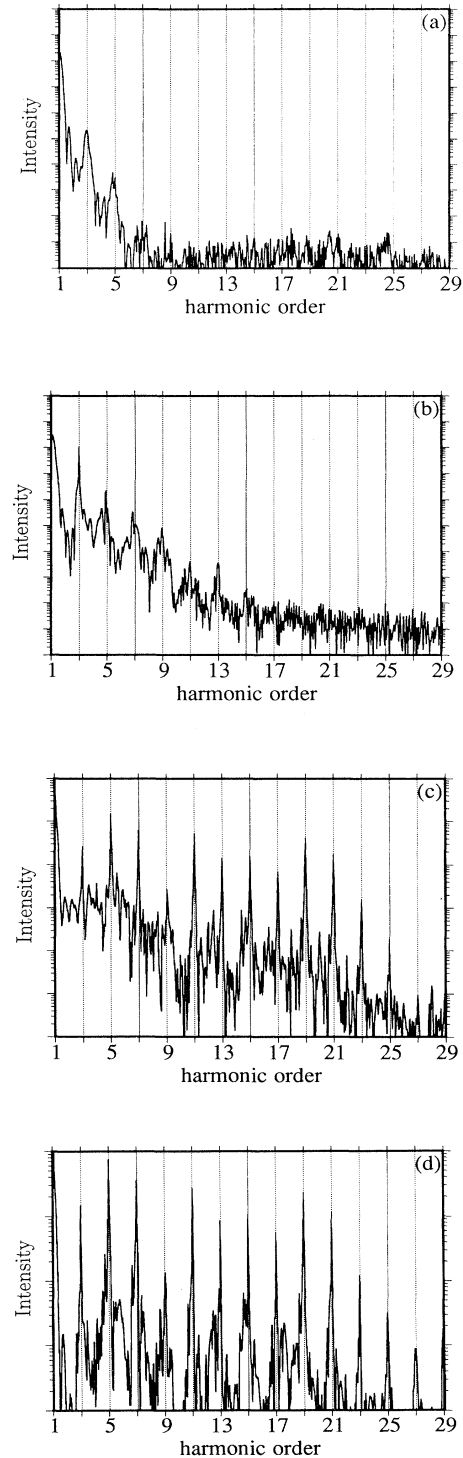


FIG. 13. The coherently scattered light spectrum as a function of the harmonic order for three different laser intensities. (a) $\mathcal{E}=0.01$ a.u. (rapid single electron detachment, no double ionization). (b) $\mathcal{E}=0.02$ a.u. (stabilized outer electron, no double ionization). (c) $\mathcal{E}=0.08$ a.u. (quickly ejected outer electron, mainly double ionization). (d) $\mathcal{E}=0.08$ a.u., the spectrum from two uncorrelated hydrogen atoms. (In all cases $\omega=0.08$ a.u., two optical cycles turn on and turn off, total pulse duration 18 optical cycles.)

[Figs. 13(a) and 13(b)] whether the features in the light spectrum could be associated with the outer or inner electron. For this higher laser intensity it is clear that essentially all spectral features come directly from the deeply bound inner electron while it gets ionized.

To make evident the effects of electron correlation at the highest field here we have repeated the last simulation with the electron-electron correlation “switched off.” This corresponds to a system described by the Hamiltonian H^0 defined in Eq. (4.1) with $G=0$. We find that there is a nearly complete one-to-one correspondence between the higher harmonics in the spectrum for the negative ion and the spectrum for two uncorrelated hydrogen atoms. This makes it quite clear that in this domain of field strengths all of the principal spectral features in the scattered light of the negative ion are due to excitation of the core electron. The higher harmonics are more distinct from the background in the case of the two uncorrelated hydrogen atoms. This might be expected on the grounds that in the latter case we have two equally active electrons producing the harmonics, compared to only one active electron during the later stages of double ionization of the negative ion. A wider investigation of the generation of higher harmonics for our two-electron system is in progress.

X. SUMMARY

We have presented a description of various aspects of a one-dimensional model two-electron quantum system characterized by the same soft-core Coulombic potential that has been used in strong-field studies of one-electron systems. We have solved Schrödinger’s equation for the fully correlated two-electron wave function for the bare atom and for the atom in the presence of a short intense laser pulse. We have calculated many low-lying bound and free eigenenergies, and the associated wave functions. A finding of particular interest is the existence of only one bound state, in common with real negative ions. On the basis of this as well as other evidence presented it appears satisfactory to interpret the model as the one-dimensional analog of a negative ion. Bare energies are similar to alkali-metal negative ions in particular. The model appears suitable as a test ground for approximate two-electron theories as well as a convenient tool to investigate the effects of a strong electron correlation on strong-field phenomena, and vice versa. In addition to bare system properties we have presented single and multiphoton detachment rates, photoelectron spectra including many ATD peaks, a brief examination of sensitive response near to channel closings, the time dependence of various core state probabilities, and scattered light spectra.

ACKNOWLEDGMENTS

We would like to thank S. L. Haan, D. Lappas, D. D. Meyerhofer, and Q. Su for many helpful discussions. This research was supported by the Division of Chemical

Sciences, Office of Basic Energy Sciences, Office of Energy Research of the U.S. Department of Energy. In addition, R.G. acknowledges the support of the Feodor Lynen Fund of the Alexander von Humboldt Foundation of Germany.

APPENDIX

Expression (8.4) can be also conveniently derived using a convenient projector formalism. The “exact” two-electron ionization probability ${}^{(2)}P(t)$ has to be defined via the energy integral over those subspace of continuum eigenstates $|\Phi_E(1,2)\rangle$ for which “both electrons are free,”

$${}^{(2)}P(t) = \int dE |\langle \Phi_E(x_1, x_2) | \Psi(x_1, x_2; t) \rangle|^2. \quad (\text{A1})$$

This is, of course, just an equivalent way of saying that ${}^{(2)}P(t)$ is the expectation value of the projector

$${}^{(2)}\hat{P} \equiv \int dE |\Phi_E(1,2)\rangle \langle \Phi_E(1,2)| \quad (\text{A2})$$

where the integration interval covers all relevant energy states. Again, the principle problem is that this corresponding submanifold $|\Phi_E(1,2)\rangle$ within all positive energy eigenstates is not uniquely determined. We propose here to replace the undetermined subspace projector ${}^{(2)}\hat{P}$ by the corresponding one for two decoupled hydrogenic states (independent particle picture)

$$\hat{P}^{(2)} \equiv \int dE \int dE' |E(1), E'(2)\rangle \langle E(1), E'(2)|, \quad (\text{A3})$$

where the state $|E(1), E'(2)\rangle$ is defined as the direct product $|E\rangle |E'\rangle$. In this notation $|E\rangle$ denotes the positive energy eigenstate of the (one-electron) hydrogen problem which can be easily computed by a straightforward diagonalization of the bare hydrogen Hamiltonian. This task is very (CPU) time consuming due to the high number of (quasi) continuous eigenfunctions. However, the complement projector to $\hat{P}^{(2)}$ is characterized by only those direct product states, in which at least one of the two states is bound. We denote the bound hydrogen states by $|n\rangle$ where $n=1, 2, 3, \dots$, is the principal quantum number. The projector $\hat{P}^{(2)}$ can then be expressed as a sum (integral) of symmetric bound-free and bound-bound components

$$\hat{P}^{(2)} = \Pi_1 \otimes \Pi_2 - \left\{ \sum_n \int dE |n(1), E(2)\rangle \langle n(1), E(2)| \right. \\ \left. + \sum_n \int dE |E(1), n(2)\rangle \langle E(1), n(2)| \right. \\ \left. + \sum_n \sum_{n'} |n(1), n'(2)\rangle \langle n(1), n'(2)| \right\}. \quad (\text{A4})$$

Here Π_i denotes the unit operator acting on the i th coordinate of the wave vector. Combining the sums and integral and making use of the completeness relation of the eigenfunctions we can simplify the above expression and find

$$\hat{P}^{(2)} = \Pi_1 \otimes \Pi_2 - \left\{ \sum_n |n(1)\rangle \langle n(1)| \otimes \Pi_2 + \sum_n \Pi_1 \otimes |n(2)\rangle \langle n(2)| - \sum_n \sum_{n'} |n(1), n'(2)\rangle \langle n(1), n'(2)| \right\}. \quad (\text{A5})$$

This expression contains only sums over discrete states

$|n\rangle$ and the expectation value of this projector can be easily computed. In principal, the sums extend to all bound states but for our parameter choice it is numerically sufficient to restrict the sum to only the 35 lowest-lying states. The evaluation of the projector can be further simplified if we take into account the symmetry of the wave function under an exchange of the electrons's coordinate. The expectation value of the projector $\hat{P}^{(2)}$ can be easily calculated in the spatial representation and we find the desired expression for the two-electron ionization probability (8.4).

- [1] For recent reviews of multiphoton phenomena, see N. B. Delone and M. V. Fedorov, *Usp. Fiz. Nauk* **158**, 215 (1989) [*Sov. Phys. Usp.* **32**, 500 (1989)]; G. Mainfray and C. Manus, *Rep. Prog. Phys.* **54**, 1333 (1991); and various articles in *Atoms in Intense Laser Fields*, edited by M. Gavrila (Academic, Orlando, 1992).
- [2] Early experimental studies of ATI include those of P. Agostini, F. Fabre, G. Mainfray, G. Petite, and N. K. Rahman, *Phys. Rev. Lett.* **42**, 1127 (1979) and P. Kruit, J. Kimman, H. G. Muller, and M. J. van der Wiel, *Phys. Rev. A* **28**, 248 (1983). Later related studies focusing on effects such as the photoelectron spectral substructure, dynamic level shifting, and resonance effects in very short pulses have been reported by and R. R. Freeman, P. H. Bucksbaum, H. Milchberg, S. Darack, D. Schumacher, and M. E. Geusic, *Phys. Rev. Lett.* **59**, 1092 (1987); P. Agostini, J. Kupersztynch, L. A. Lompre, G. Petite, and F. Yergeau, *Phys. Rev. A* **36**, 4111 (1987); M. P. de Boer and H. G. Muller, *Phys. Rev. Lett.* **68**, 2747 (1992); G. N. Gibson, R. R. Freeman, and T. J. McIlrath, *Phys. Rev. Lett.* **69**, 1904 (1992). For reviews of this area of multiphoton physics, see P. Agostini and G. Petite, *Contemp. Phys.* **29**, 57 (1988); J. H. Eberly, J. Javanainen, and J. H. Eberly, *Phys. Rep.* **204**, 331 (1991); and R. R. Freeman and P. H. Bucksbaum, *J. Phys. B* **24**, 325 (1991).
- [3] A. McPherson, G. Gibson, H. Jara, U. Johan, I. A. McIntyre, K. Boyer, and C. K. Rhodes, *J. Opt. Soc. Am. B* **4**, 595 (1987); M. Ferray, A. L'Huillier, X. F. Li, L. Lompre, G. Mainfray, and C. Manus, *J. Phys. B* **21**, L31 (1988); X. F. Li, A. L'Huillier, M. Ferray, L. A. Lompre, and G. Mainfray, *Phys. Rev. A* **39**, 5751 (1989); A. L'Huillier and P. Balcou, *Phys. Rev. Lett.* **70**, 774 (1993); J. J. Macklin, J. D. Kmetc, and C. L. Gordon III, *ibid.* **70**, 1327 (1993).
- [4] V. V. Suran and I. P. Zapesochnyi, *Pis'ma Zh. Tekh. Fiz.* **1**, 973 (1975) [*Sov. Tech. Phys. Lett.* **1**, 420 (1975)]; I. Aleksakhin, I. P. Zapesochnyi, and V. V. Suran, *Pis'ma Zh. Eksp. Teor. Fiz.* **26**, 14 (1977) [*JETP Lett.* **26**, 11 (1977)]; A. L'Huillier, L.-A. Lompre, G. Mainfray, and C. Manus, *Phys. Rev. Lett.* **48**, 1814 (1982); *Phys. Rev. A* **27**, 2503 (1983); T. S. Luk, H. Pummer, K. Boyer, M. Shahidi, H. Egger, and C. K. Rhodes, *Phys. Rev. Lett.* **51**, 110 (1983).
- [5] S. Augst, D. Strickland, D. D. Meyerhofer, S. L. Chin, and J. H. Eberly, *Phys. Rev. Lett.* **63**, 2212 (1989); G. Gibson, T. S. Luk, and C. K. Rhodes, *Phys. Rev. A* **41**, 5049 (1990).
- [6] K. Kulander, *Phys. Rev. A* **35**, 445 (1987); **36**, 2726 (1987); **38**, 778 (1988).
- [7] J. Javanainen, J. H. Eberly, and Q. Su, *Phys. Rev. A* **38**, 3430 (1988).
- [8] J. Javanainen and J. H. Eberly, *J. Phys. B* **21**, L93 (1988); J. Javanainen and J. H. Eberly, *Phys. Rev. A* **39**, R458 (1989).
- [9] R. Grobe, C. I. Moore, Q. Su, W. G. Greenwood, and J. H. Eberly, *Ann. Phys. (Leipzig)* **7**, 87 (1991).
- [10] M. S. Pindzola, D. C. Griffin, and C. Bottcher, *Phys. Rev. Lett.* **66**, 2305 (1991).
- [11] M. Dörr, D. Feldmann, R. M. Potvliege, H. Rottke, R. Shakeshaft, K. H. Welge, and B. Wolff-Rottke, *J. Phys. B* **25**, L275 (1992).
- [12] A. L'Huillier, P. Balcou, S. Candel, K. J. Schafer, and K. C. Kulander, *Phys. Rev. A* **46**, 2778 (1992).
- [13] For discussions of strong field stabilization, see *Atoms in Intense Laser Fields*, edited by M. Gavrila (Academic, Orlando, 1992), and the special issues of *J. Opt. Soc. Am. B* **7** (4), 1990, and *Laser Phys.* **3** (2), (1992).
- [14] F. H. M. Faisal and P. Scanzano, *Phys. Rev. Lett.* **68**, 2909 (1992).
- [15] D. Proulx and R. Shakeshaft, *Phys. Rev. A* **46**, R2221 (1992).
- [16] C. R. Liu, B. Gao, and A. F. Starace, *Phys. Rev. A* **46**, 5985 (1992).
- [17] R. Grobe and J. H. Eberly, *Phys. Rev. Lett.* **68**, 2905 (1992).
- [18] R. Grobe and J. H. Eberly, *Phys. Rev. A* **47**, R1605 (1993).
- [19] R. Grobe and J. H. Eberly, *Laser Phys.* **3**, 323 (1993).
- [20] R. Grobe and J. H. Eberly, *Phys. Rev. A* **48**, 623 (1993).
- [21] For the fundamental physics of negative ions, see H. Massey, *Negative Ions* (Cambridge University Press, Cambridge, 1976). For overviews of negative ions and their response to weak fields, see P. A. Golovinskii and I. Yu. Kiyani, *Usp. Fiz. Nauk* **161**, 97 (1990) [*Sov. Phys. Usp.* **33**, 453 (1990)], and C. A. Nicolaidis, Th. Mercouris, and G. Aspromallis, *J. Opt. Soc. Am. B* **7**, 494 (1990).
- [22] For a review, see C. D. Lin, *Adv. At. Molec. Phys.* **22**, 77 (1986).
- [23] J. H. Eberly, *Am. J. Phys.* **33**, 771 (1965).
- [24] M. D. Feit, J. A. Fleck, Jr., and A. Steiger, *J. Comput. Phys.* **47**, 412 (1982).
- [25] For a generalization of the split-operator method to higher orders, see A. D. Bandrauk and H. Shen, *Chem. Phys. Lett.* **176**, 428 (1991).
- [26] Properties of the Hanning window are discussed in W. H. Press, B. P. Flannery, S. A. Teukolsky, and W. T. Vetterling, *Numerical Recipes* (Cambridge University Press, Cambridge, 1986).
- [27] For a related method to obtain spectra, see K. J. Schafer and K. C. Kulander, *Phys. Rev. A* **42**, 5794R (1990) and

- K. J. Schafer, *Comput. Phys. Commun.* **63**, 427 (1991).
- [28] For structural properties of the one-dimensional soft-core hydrogen atom see Q. Su and J. H. Eberly, *Phys. Rev. A* **44**, 5997 (1991) and J. H. Eberly, *ibid.* **42**, 5750 (1990).
- [29] The hydrogen negative ion is the only negative ion for which the existence of only one bound state has been proven rigorously, R. N. Hill, *Phys. Rev. Lett.* **38**, 643 (1977).
- [30] A. Macias and A. Riera, *Phys. Rev. A* **40**, 4298 (1989); E. dePrunele, *ibid.* **45**, 2070 (1992) and references therein.
- [31] S. L. Haan, R. Grobe, and J. H. Eberly (unpublished).
- [32] This pulse shape is very convenient because it combines a rapid turn on and turn off with the drift-free motion of a free electron that is typical for a truly adiabatic pulse; see R. Grobe and M. V. Fedorov, *J. Phys. B* **26**, 1181 (1993).
- [33] For a discussion of the gauge in intense laser fields, see Ref. 32.
- [34] For related methods to eliminate interactions with the boundary, see D. Neuhauser and M. Baer, *J. Chem. Phys.* **90**, 435 (1989); C. W. McCurdy and C. K. Stroud, *Comput. Phys. Commun.* **63**, 323 (1991).
- [35] For a nice review of multiphoton detachment rates for short-range potentials, see S. Geltman, *Phys. Rev. A* **43**, 4930 (1991).
- [36] S. M. Susskind, S. C. Cowley, and E. J. Valeo, *Phys. Rev. A* **42**, 3090 (1990).
- [37] W. G. Greenwood and J. H. Eberly, *Phys. Rev. A* **43**, 525 (1991).
- [38] G. Scharf, K. Sonnenmoser, and W. F. Wreszinski, *Phys. Rev. A* **44**, 3250 (1991).
- [39] J. H. Eberly, *J. Phys. B* **23**, L619 (1990).
- [40] F. H. M. Faisal, *Multiphoton Processes* (Plenum, New York, 1987).
- [41] C. Y. Tang, P. G. Harris, A. H. Mohagheghi, H. C. Bryant, C. R. Quick, J. B. Donahue, R. A. Reeder, S. Cohen, W. W. Smith, and J. E. Stewart, *Phys. Rev. A* **39**, R6068 (1989).
- [42] To relate to the previous discussion in Sec. VI we choose here the same low frequency $\omega=0.04$ a.u. A lower frequency is more expensive in terms of CPU time and memory requirements. The large optical period, $2\pi/\omega=50\pi$, requires many hundreds of integration steps per cycle and the corresponding long integration time requires a rather large spatial box. A large box size L is also necessary for long integration times to decrease the finite spacings between two neighboring continuum eigenstates which could lead to unphysical oscillation. These technical restrictions allow us to compute the spectra for only very short pulses in terms of optical cycles.
- [43] Q. Su and J. H. Eberly, *Laser Phys.* **2**, 598 (1992).
- [44] D. G. Lappas, R. Grobe, and J. H. Eberly (unpublished).